Available online at www.sciencedirect.com
SCIENCE DIRECT®
Journal of Solid State Chemistry 177 (2004) 4706–4723
JOURNAL OF SOLID STATE CHEMISTRY
www.elsevier.com/locate/jssc

On the structural defects in synthetic γ-MnO_2s

L.I. Hill, A. Verbaere*

Laboratoire de Chimie des Solides, Institut des Matériaux Jean Rouxel, Universite de Nantes et CNRS UMR 6502, rue de la Houssinière, BP 32229, 44322 Nantes Cedex 03, France

Received 22 July 2004; received in revised form 26 August 2004; accepted 27 August 2004

Abstract

In the literature, the γ-MnO_2 structure is considered to be that of ramsdellite (R), in which two types of defects exist. The occurrence of a slab of pyrolusite (r) is named a De Wolff defect and random faults r in R give intergrowths of ramsdellite and pyrolusite, which account well for the global features of many experimental diffraction patterns. The other type of defect results from ''microtwinning'', which allows the so-called ε-MnO_2 to be put with γ-MnO_2 in the same classification. This paper discusses the previous models of defect and what could be the features of the ''microtwinning'', giving for each possible model the corresponding expected features in reciprocal space. The results of a selected area electron diffraction study of rather well crystallized samples of γ-MnO_2 are presented. The splitting of particular diffraction spots and new diffuse intensity are interpreted as the first experimental evidence for ''microtwinning'', and a model with orientation variants within microdomains embedded in a ''normal'' structure is proposed, which is rather different from the previous hypotheses involving parallel twin planes and parallel twin boundaries.

Keywords: Gamma manganese dioxide; γ manganese dioxide; Ramsdellite; Pyrolusite; Defect structure; Microtwinning; Electron diffraction

1. Introduction

The γ-MnO_2 compounds called chemical manganese dioxide (CMD), electrochemical manganese dioxide (EMD), or heat-treated CMD or EMD (HTMD) have structures which derive from that of ramsdellite (or that of pyrolusite, β-MnO_2) by introducing structural defects. Thus the usual methods of characterization and study by powder X-ray diffraction (PXRD) cannot be followed, and they are replaced by comparisons of the experimental PXRD patterns with either a set of IBA reference patterns [1] or patterns calculated introducing defects in the ramsdellite (R) or pyrolusite (r) structures [2–5]. On the latter approach, important, basic progress was provided by the article published in 1995 by Chabre and Pannetier [2]. A number of aspects (including a review on manganese dioxides) are dealt with in this long, detailed article. The present paper uses the same notations and symbols as in [2].

After the work by De Wolff [6], the γ-MnO_2 structure has been considered as an intergrowth of ramsdellite (R) and pyrolusite (r), i.e., as faults r in R (Fig. 1). The parameter Pr was introduced as the fraction of slabs r in the structure. Pr is also the probability of an r fault, called a ''De Wolff defect'', which consists of the occurrence of a single chain of octahedra instead of double chains. The other parameter, Tw, [2] was introduced to give a percentage of ''microtwinning'', the twinning involved (Fig. 2) being a change of ca. 60/120° in the *c*-axis direction (here the space group *Pbcm* is used for R and this setting is retained for a faulted R).

In subsequent works, [3–5] the classification of γ-MnO_2s was still done using two parameters for the defects; however, the parameter Tw was replaced by a similar one, Mt, for which the distribution of the twin planes is different, compared to Tw. In addition, the classification by (Pr, Mt) is based on supplementary

*Corresponding author. Fax: +33-2-40-37-39-95.
E-mail address: alain.verbaere@cnrs-imn.fr (A. Verbaere).

0022-4596/$ - see front matter © 2004 Elsevier Inc. All rights reserved.
doi:10.1016/j.jssc.2004.08.037

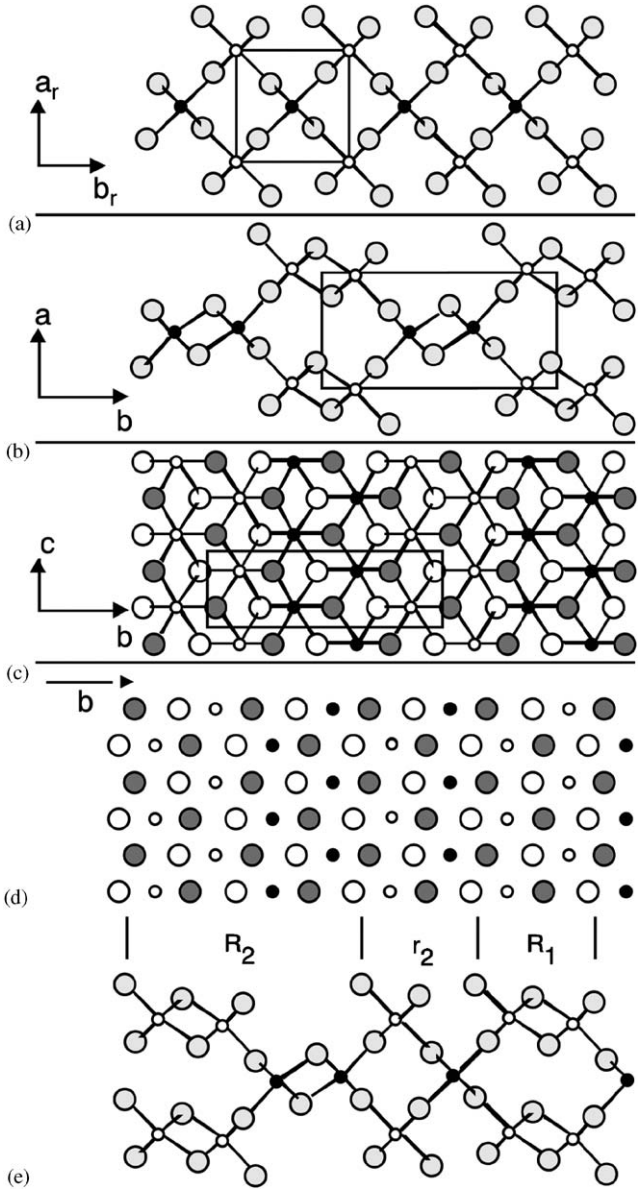

Fig. 1. Structures of pyrolusite r (a), and ramsdellite R (b), (c). Open and filled small circles represent Mn atoms at x close to 0 and $\frac{1}{2}$, respectively. (d) (e): schematic [100] (d) and [001] (e) views of a R–r intergrowth. R_n or r_n indicates a succession of n consecutive slabs R or r, respectively.

calculated PXRD patterns, and its applicability is for low microtwinning rates [5].

The De Wolff defects explain well numerous features observed in diffraction patterns of γ-MnO_2. For instance, the particular shifts expected by De Wolff [6] were observed in selected area electron diffraction (SAED) patterns [7] and HRTEM images of De Wolff defects were actually observed [8]. It is still difficult, in contrast, to imagine what the microtwinning is.

Various manganese dioxides (MDs) were electrochemically deposited in our group using hydrothermal

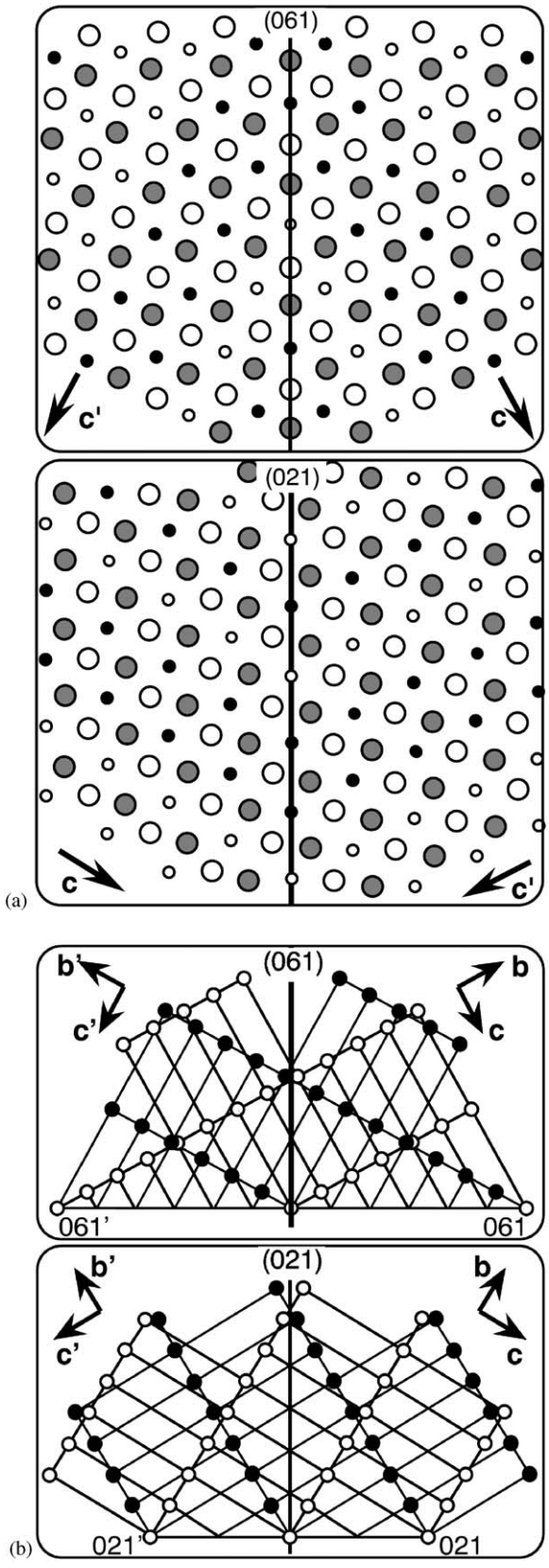

Fig. 2. Schematic [100] view of ideal (021) and (061) twinning in γ-MnO_2, when the interface coincides with the twin plane. Note that the changes of the direction of the chains of octahedra result from a different occupancy of the octahedral sites (a). Corresponding reciprocal lattices of the orientation variants (b).

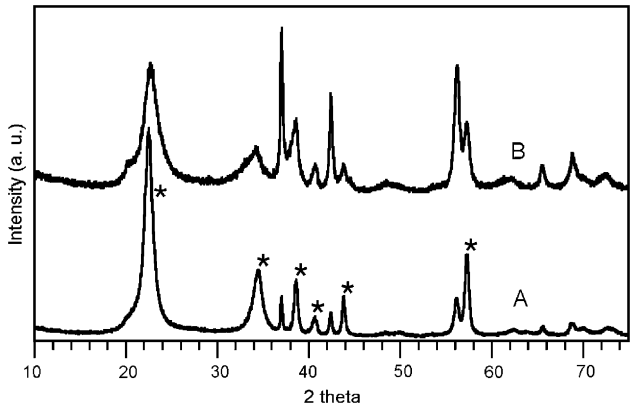

Fig. 3. PXRD patterns of two typical samples: A, the marked needle-shaped morphology has provoked a preferred orientation enhancing reflections with $l = 0$ (*); Pr = 0.38, Tw = 22, Mt = 20. B, pattern similar to that of IBA 11; Pr = 0.44, Tw = 26, Mt = 24.

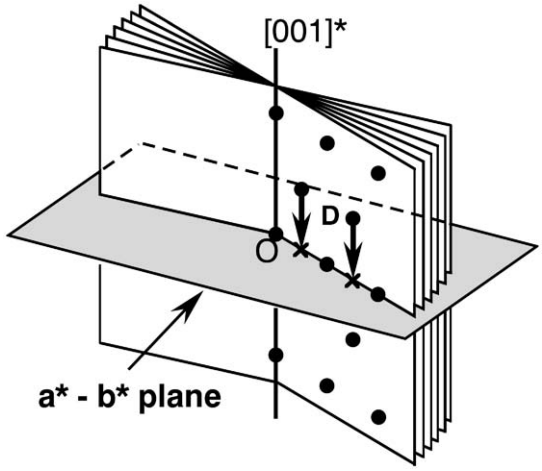

Fig. 4. Study of the reciprocal space: illustration of the rotation during the study and of the representation of the intensity by projection (arrows D).

conditions [4,5,9], and some are γ-MnO_2 giving "line-rich" PXRD patterns rather similar to those of CMDs, or that of an EMD obtained at low deposition current density (DCD). They consist of well-formed, needle shaped crystals. Fig. 3 shows typical PXRD patterns for these compounds. As their crystallinity is relatively good, they were selected for a systematic SAED study, to eventually detect microtwinning.

This paper first presents and discusses the previous models of defects in γ-MnO_2s, and what could be the features of the "microtwinning", giving for each model the main features expected in reciprocal space. Then the SAED results are presented and discussed.

2. Experimental

The EMD samples were prepared by hydrothermal–electrochemical synthesis described in detail in [9], from acidic $MnSO_4$ solutions (pH in the range 0–4), at 92 °C.

All the PXRD patterns considered (experimental or calculated) correspond to Cu$K\alpha$ radiation. The calculated PXRD patterns were obtained using the programs Powdercell [10] or Diffax [11], with pseudo-Voigt line profiles arbitrarily selected to facilitate comparisons with the experimental patterns of most of the γ-MnO_2. In this paper, the axes and the indices will usually refer to the orthorhombic unit cell of ramsdellite, R, with use of the setting consistent with space group *Pbnm* (No. 62) with $a = 4.53$ Å, $b = 9.27$ Å, $c = 2.866$ Å, [12] but sometimes the subscript H will indicate that an hexagonal unit-cell is used, with $a_H \approx 2.80$ Å and $c_H \approx 4.45$ Å (this is the cell commonly associated with ε-MnO_2). In the same manner, subscript r will correspond to the tetragonal axes of pyrolusite β-MnO_2.

The SAED study was performed using a CM30 electron microscope operating at 300 kV. For each sample, several crystals were studied under weak irradiation by systematic rotation about the *c*-axis, which always coincided with the largest crystal dimension (generally the axis of the needle shaped crystals). The rotation axis $\vec{c}*$ was rather easy to recognize and to keep visible in the SAED pattern, since reflection 0 0 2 is intense. Whatever the pattern upon rotation, a photograph was taken after every rotation of 3°, in an explored angular range as large as possible (generally 40–50°). Fig. 4 illustrates the method, showing how each reciprocal lattice was built from the photographs by projecting the observed spots onto the (a*, b*) plane. As shown in Fig. 4, a cross and a disk, in this projection, represent a spot (resulting either from a reciprocal lattice point or from diffuse intensity due to the defects) at l odd and l even, respectively.

3. On the previous models of defects in γ-MnO_2s

3.1. De Wolff defects

These defects were proposed by De Wolff [6], who described and discussed their effects in reciprocal space. His model assumed defects were always isolated from each other and predicted particular shifts of some reciprocal lattice points, parallel to the *b*-axis. Other distributions of the same defects (i.e., possibility of occurrences of thicker slabs having the rutile type structure) were then considered: Chabre and Pannetier [2] calculated, with the program Diffax, the PXRD patterns expected for the random distribution of r for various Pr values; S. Sarciaux [3] extended the calculation of PXRD patterns, considering all distributions at

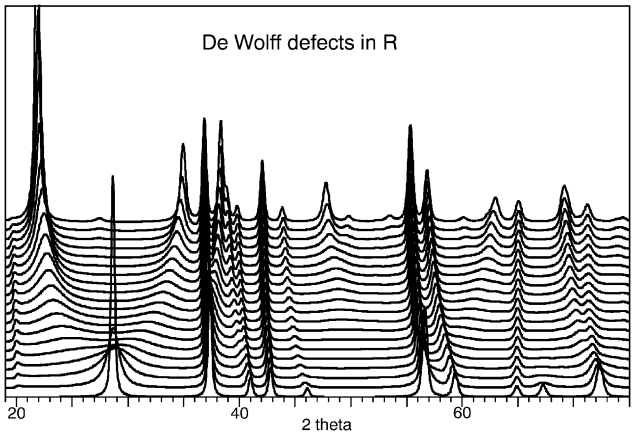

Fig. 5. PXRD patterns calculated by introducing De Wolff defects in R (top and bottom for Pr = 0.05 and 1, respectively; step of 0.05).

each Pr (i.e., considering all possible values of the probabilities of sequence R–R and r–r at a given Pr value). Fig. 5 is shown to illustrate the practical effects in the case of random defects.

3.2. Microtwinning

Considering that the patterns of Fig. 5 do not fully explain many of the experimental ones, Chabre and Pannetier [2] introduced defects of "microtwinning", stating that there is the theoretical possibility of a continuous evolution from a γ-MnO_2 with only De Wolff defects to an "ε-MnO_2", where the symmetry becomes hexagonal due to an extreme twinning (the twinning not being dependent on the De Wolff defects). At this latter limit, the double chains of R and/or single chains of r running parallel to the c-axis (Fig. 2) undergo so many changes of direction at ca. 60/120° upon twinning that a mean hexagonal structure results. [2] The parameter Tw gives the degree of microtwinning, by considering the two following approaches:

i. Tw varies linearly from 0% to 100% where microtwinning increases from 0 to the hexagonal limit; the evolution is supposed to be marked by the regular increase of the ratio $b/(2c)$ up to $\sqrt{3}$. This ratio is the effective ratio inferred from selected line positions in the PXRD pattern [2].
ii. The effects of twinning are obtained by calculations of PXRD patterns with the program Diffax [11], introducing (021) twin planes. These parallel planes are supposed to be perpendicular to the direction of crystal growth [2].

These two approaches are completely different, since with (i) the line shifts result from changes in the parameters of periodicity, while for (ii) these parameters are constant. However, they were supposed to be consistent with each other, and similar, which allowed both γ- and ε-MnO_2 to be put into a single classification by (Pr, Tw).

The other classification proposed for γ-MnO_2 [3–5] results from further calculations of PXRD patterns. For instance, it was verified that (061) twin planes give effects similar to (021) planes, in the PXRD pattern. In the classification, the microtwinning parameter Mt corresponds to a different probability law for the occurrence of twinning, compared to Tw. However, the simulations still result from planar, parallel faults.

3.3. On the spatial distribution of De Wolff defects

As illustrated by Fig. 5, the Pr value is easily estimated from the experimental line positions (or linewidth), mainly in the angular range $21° < 2\Theta < 35°$. In fact, the result is slightly influenced by the De Wolff defect distribution [3]. Fig. 6 allows one to compare two cases: in Fig. 6(a), the De Wolff defects are always isolated; in Fig. 6(b), they are randomly distributed. At Pr = 0.5, Fig. 6(a) corresponds to a perfectly ordered compound, where the r and R slabs (Fig. 1) alternate. As the four possible successions of slabs R and r are R–R, R–r, r–R or r–r, the compound is obtained by the succession probabilities $P_{R-R} = P_{r-r} \approx 0$ and $P_{R-r} = P_{r-R} \approx 1$ (for more details, see Refs. [2,3]). The line shifts of Fig. 6 correspond well to the predictions of De Wolff [6], which are also described in [2,7]. The hypothetical, ordered MnO_2 at Pr = 0.5 (HOMD) exhibits PXRD lines whose intensity is unusual for a γ-MnO_2, for instance at ca. $2\Theta = 20°, 50°, 61°$. Note also

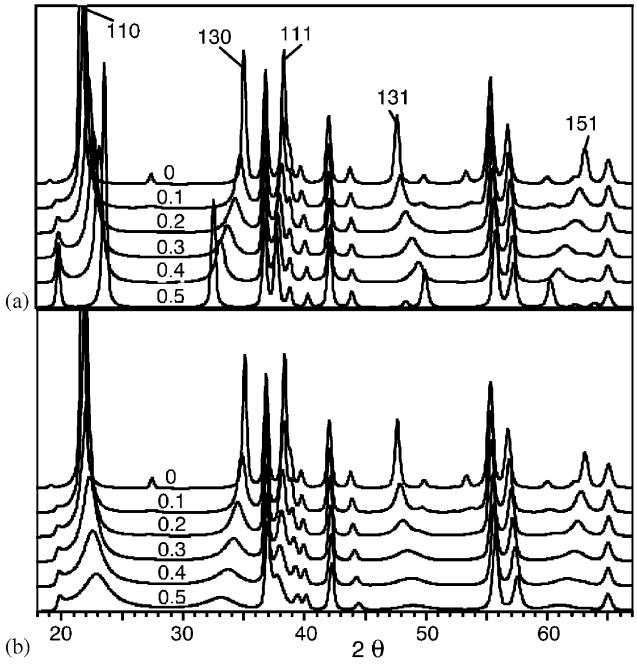

Fig. 6. PXRD patterns calculated by introducing, in R, De Wolff defects: (a) always isolated from each other; (b) at random. The value of Pr is indicated.

Table 1
Crystal data used to calculate the expected PXRD pattern of the HOMD (hypothetical, ordered γ-MnO_2 at Pr = 0.5)

Atom	x/a	y/b	z/c
Mn(1)	0.0000	0.0000	0.0000
Mn(2)	0.6610	0.0000	0.5060
O(1)	0.4465	0.0000	0.7680
O(2)	0.8905	0.0000	0.2600
O(3)	0.7830	0.0000	0.7260

Space group $C2/m$ (No. 12); $Z = 6$; cell parameters: $a = 13.7$ Å; $b = 2.867$ Å; $c = 4.46$ Å; $\beta = 90.5°$.

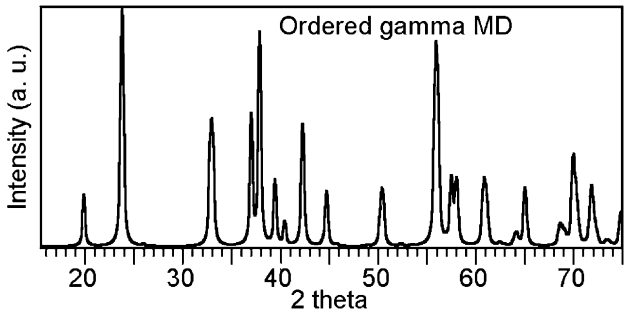

Fig. 7. PXRD pattern expected for the HOMD. Crystal data from Table 1 and a constant FWHM of 0.39° (pseudo-Voigt profile) were used.

that the lines at ca. 24° and 33° are intense, i.e., they are not expected to correspond to "superstructure" reflections (usually weak) in an X-ray or electron diffraction pattern. It is not obvious, therefore, to accept the previous conclusions or hypothesis stating that the weak superstructure spots in Fig. 1(b) in [7] and Fig. 4 in [13] are Bragg spots from the HOMD, since they just correspond to two PXRD lines which are among the strongest ones in Fig. 6(a).

In fact, when one tries to build the perfect HOMD structure using alternating slabs of R and r, obtaining acceptable interatomic distances, the crystal data given in Table 1 are obtained. With these data, all the Mn–O bond lengths are in the range 1.908–1.912 Å. Since the β value is close to 90°, the monoclinic unit-cell in Table 1 is not very different from the orthorhombic one implicitly involved in the previous studies [2,3]. The calculated PXRD pattern of the monoclinic HOMD is presented in Fig. 7. Note that a few random defects in the R–r–R–r… alternation imply (i) an overall orthorhombic symmetry, despite the local symmetry being monoclinic, and (ii) some line broadenings which are easy to predict, qualitatively, by considering the evolutions from Figs. 6(a) to 6(b), for Pr = 0.5.

3.4. On the spatial distribution of the twin planes

In the previous PXRD calculations [2,3], there was only one kind of twin plane (say (021)) and thus only

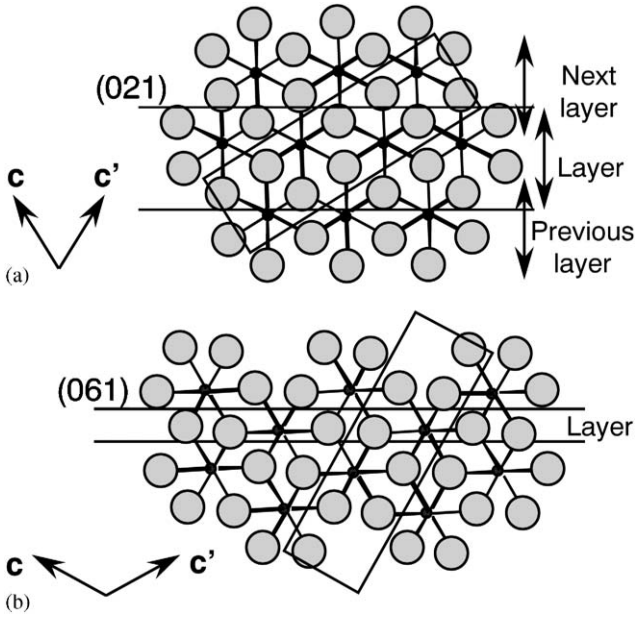

Fig. 8. [100] view of the slab giving layer 1 or 2 in R (see also Fig. 2) for (a) (021) twinning, (b) (061) twinning. The large circles represent oxygen atom positions (some of the occupancy factors of which are $\frac{1}{2}$ to avoid double occupancy after stacking).

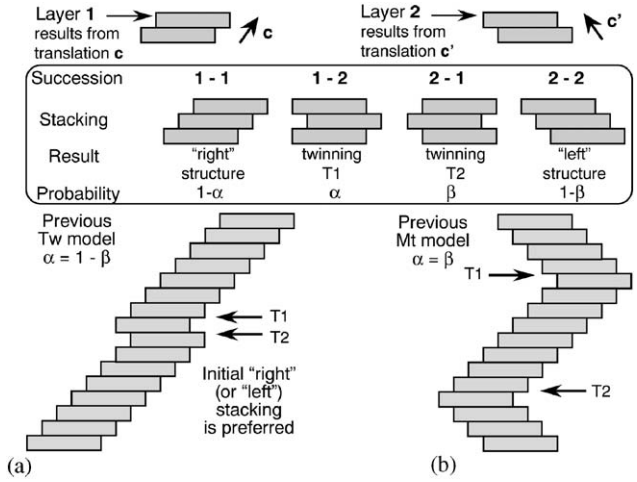

Fig. 9. Schematic illustration of the twinning T1 or T2 and of the two previous models. The "right" and "left" structures are equivalent.

parallel twin planes, due to the features of the program Diffax, which requires that the whole structure results from a stacking of compatible layers in only one stacking direction. Fig. 8 illustrates the process, showing the layers and their stacking, which may be used to obtain (021) or (061) twinning in R. The corresponding twinning in r is similar (with twin planes $(011)_r$ or $(031)_r$). Fig. 9 shows how a stacking of the layers 1 and/or 2 (which are identical slabs) can give either the structure or various occurrences of "parallel" twinning therein. The figure also gives a definition of the probabilities α and β of the two possible twinning cases

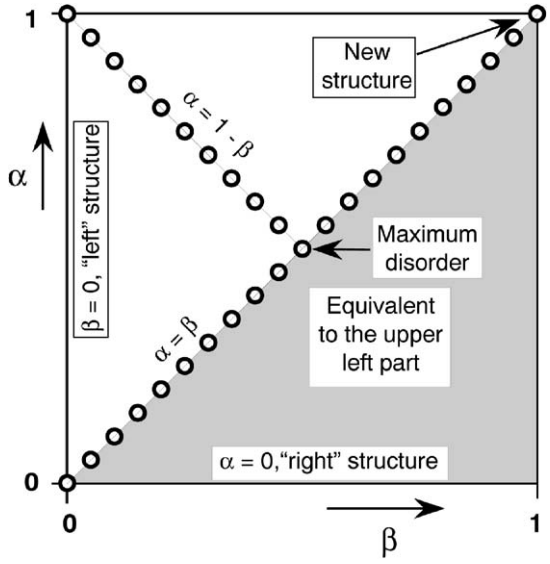

Fig. 10. Probability diagram. Open circles indicate the probabilities of parallel twinning for which PXRD patterns have been calculated [2,3].

T1 and T2, and it illustrates the difference between the distributions of T1 and T2 used in the previous "Tw model" [2] and "Mt model" [3]. Fig. 10 presents a diagram of probability, in which the two diagonals correspond to these two models, each with a particular relationship between α and β. When $\alpha = 1-\beta$, the structures are equivalent at $\alpha = x$ and at $\alpha = 1-x$, and the maximum disorder is reached at $\alpha = 1-\beta = \frac{1}{2}$, i.e., at Tw = 100 [2]. Thus the structure is always far from the complete, systematic twinning, a feature which was not really seen in [2]. When $\alpha = \beta$, complete twinning can be reached, at $\alpha = 1$, i.e., at Mt = 100, thus really allowing one to obtain for instance the α-PbO_2 type structure by systematic $(011)_r$ twinning in pyrolusite [3].

3.5. Some problems with the previous models of microtwinning

In the classification by (Pr, Tw), Tw is determined by the degree of increase of the ratio $b/(2c)$. At Tw = 0, the ideal value of $b/(2c)$ for γ-MnO_2 (thus not only for R) was supposed to be that for R (1.617), the maximum being 1.732 (due to maximum microtwinning, which gives a hexagonal symmetry and $b/(2c) = \sqrt{3}$). However, in perfect r the corresponding ratio is $b_r/c_r = 1.531$, so that if the microtwinning is weak or negligible the ratio decreases from R to r, thus giving a meaningless, negative value of Tw. This is the case for the usual HTMDs.

The classification by (Pr, Mt) has the advantage of being able to also classify a HTMD. The disadvantages are:

a) the classification is based on calculations for which several crucial parameters were arbitrarily fixed, in particular parameters of periodicity, and

b) the classification of heavily twinned structures is not possible.

3.6. Atomic shifts in the case of defect

All the γ- or ε-MnO_2 are supposed to have, at least approximately, a hexagonal close packing arrangement of the oxygen atoms, in which half of the octahedral sites are occupied by Mn. A perfect or quasi-perfect alternation of empty and occupied octahedral sites along the a-axis (which becomes the c_H axis in "ε-MnO_2") is necessary to avoid strong repulsion between close, adjacent Mn [2,14]. Thus the structure considered here and its defects are mainly characterized by the x (or z_H) coordinates of the Mn atoms. For instance, the change from an R to an r slab is mostly the change $\Delta x \approx \frac{1}{2}$ for rows of Mn atoms (Fig. 1). The same is true for twinning (021) or (061) (Fig. 2(a)). By comparing the Mn positions in R and r, one expects that such a Δx change is associated with other atomic shifts. For instance, on going from r to R, a shift of a Mn row of ca. 0.4 Å is observed parallel to the (b, c) plane. This shift ensures acceptable Mn–Mn distances between neighboring cations when their x coordinates become equal (this is the major reason why parameter b is slightly greater than $2b_r$, see Fig. 1).

Let us neglect the detail of the oxygen atom locations, as they are less sensitive to the defects considered. With respect to a perfect structure, the defects provoke changes $\Delta\phi$ in the phases ϕ of the waves scattered, during a diffraction experiment, by Mn rows parallel to [100]. Let us express the amplitude of a wave scattered by a given atom, with atomic scattering factor f_q and with fractional coordinates x y z, as:

$$f_q \exp[i\phi] = f_q \exp[2\pi i(hx + ky + lz)].$$

For a relevant Mn row, a defect provokes changes Δx, Δy, Δz of the fractional atomic coordinates, and the change of phase ϕ is

$$\Delta\phi = 2\pi(h\Delta x + k\Delta y + l\Delta z),$$

where $\Delta x \approx \frac{1}{2}$. Note that Δx is much greater than Δy and Δz. When h is odd ($h = 2n+1$), the defect implies a strong phase change ($\Delta\phi \approx \pi + 2n\pi$) likely modifying the X-ray or electron diffraction pattern considered. For h even, the value of $h\Delta x$ being close to an integer, the expected effects are much smaller, as they are mainly due to the small Δy and Δz.

An illustration of the above remark is given by Fig. 6 in Ref. [15], which shows SAED patterns of γ- or ε-MnO_2 crystallites: a SAED pattern from a CMD is shown in Fig. 6a in [15], and it looks like the $[001]_H$ zone from a perfectly hexagonal ε-MnO_2, whereas, after rotations about reciprocal $[100]_H$*, patterns clearly show

diffuse intensity (in particular in Fig. 6c in [15], where streaks due to De Wolff defects appear). The $[001]_H$ zone of ε-MnO_2 corresponds to the [100] zone for γ-MnO_2, i.e., to $h = 0$ (even); the diffuse intensity revealing the defects appears at $h = 1$ (odd). As will be seen in a following section, our SAED studies of γ-MnO_2 agree with these features, showing that the diffuse intensity mainly concerns the reciprocal planes at $h = 2n + 1$, and that it is weak (may not be visible) for $h = 2n$. Note that the previous results are therefore questionable when they infer a structural conclusion concerning a γ- or ε-MnO_2 crystallite from a single electron diffraction pattern of a [100] or $[001]_H$ zone.

4. What could be "microtwinning" in γ- and ε-MnO_2

4.1. "True ε" and hexagonal compounds—the first limit

According to the discussion in [2], we use hereafter the label "true ε" for the truly hexagonal structure of MD first described by De Wolff [14], with $a_H \approx 2.80$ Å and $c_H \approx 4.45$ Å. It is a hypothetical, mean structure of the NiAs type, in which the Mn atoms occupy the octahedral sites with the mean occupancy factor of $\frac{1}{2}$. Mn atoms and vacancies are supposed to perfectly alternate along the c_H-axis, and each resulting Mn row corresponds to either $z_H = 0$ or $z_H = \frac{1}{2}$ for the Mn location (it would correspond to $x \approx 0$ or $x \approx \frac{1}{2}$ in R or r, the row being parallel to the a- or a_r-axis, see Fig. 1). As the two possibilities are supposed to be present at random for all the Mn rows, a complete disorder results parallel to the (a_H, b_H) plane. Further aspects of this "true ε" MD are discussed in Ref. [2]. Fig. 11(a) is inferred from Fig. 10 in [2]. It illustrates the features of the calculated PXRD pattern of the "true ε" MD. It is that typical of an EMD prepared at high DCD, where the broad line or the bump at $2\theta \approx 22°$ (which is the one not explained by the hexagonal cell, see Figs. 11(b), (c) near 22°) would be replaced by a step-shaped diffuse intensity, starting at $2\theta \approx 20°$ and decreasing slowly toward higher angles. The latter diffuse intensity results from the situation of partial order (1D order) and partial disorder (2D disorder), which implies, in reciprocal space, diffuse intensity planes perpendicular to the c_H-axis at l_H = integer, except 0. The step at $2\theta \approx 20°$ corresponds to the first plane, at $l_H = 1$ [2], which becomes $h = 1$ in γ-MnO_2.

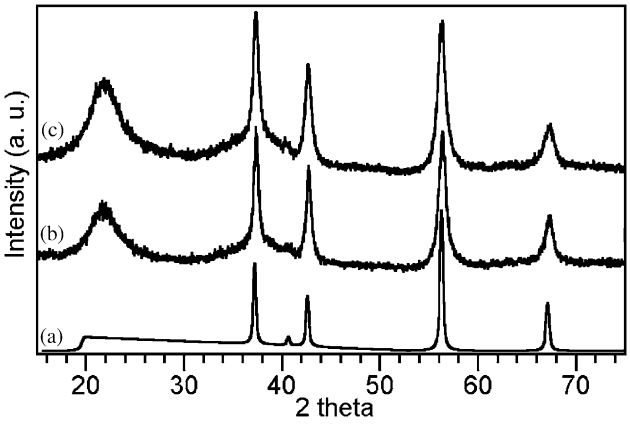

Fig. 11. PXRD patterns: (a) expected for the "true ε" (pattern inferred from Fig. 10 in Ref. [2], which assumes 1D order for Mn in a NiAs structure); (b) and (c) for EMD samples deposited at high DCD in our group.

We suppose that a so-called "ε-MnO_2" does exhibit a broad line or bump at $2\theta \approx 22°$ (i.e., a feature here which is different from the step-shaped intensity calculated for the "true ε", see Fig. 11) due to the introduction of short-range order (SRO) for Mn in the structure of the hexagonal "true ε MnO_2". This model with 1D order and 2D SRO likely corresponds to the extreme limit of microtwinning in the known γ-MnO_2. At this limit, we expect a hexagonal symmetry in reciprocal space and also in real space at the scale of 1 nm or even less. Diffuse intensity planes must result in reciprocal space, in particular for l_H odd (i.e., h odd), and in these planes the particular features of the intensity depend on the features of the SRO.

4.2. (021) and (061) macrotwinning—the other limit

Let us simply consider R, thus ignoring the possible presence of De Wolff defects, since $(011)_r$ or $(031)_r$ twinning in r is similar to (021) or (061) twinning in R. The limit corresponds to "crystals" in which one or a few planar boundaries parallel to (021), (02−1), (061), and/or (06−1) separate twin domains (see Fig. 2). Each resulting orientation variant is large enough (at least ca. 20 or 30 nm) so that its features (in particular the cell parameters) are not significantly influenced by the presence of the adjacent neighboring domains (the influence concerns only the atoms close to a boundary). Two adjacent domains are supposed to have a precise relative orientation fully determined by the features of the boundary. Figs. 2 and 12 correspond to ideal twinning.

Here, the expected PXRD pattern should be practically that of the untwinned structure, with some line broadening mainly determined by the size of the domains. The SAED patterns from a "crystal" should simply result from the addition of the reciprocal lattices of the few orientation variants, without visible streaks.

4.3. Intermediate cases

Between high microtwinning (up to SRO and hexagonal symmetry) and macrotwinning, we expect to find the cases of the synthetic γ-MnO_2s, which give "line

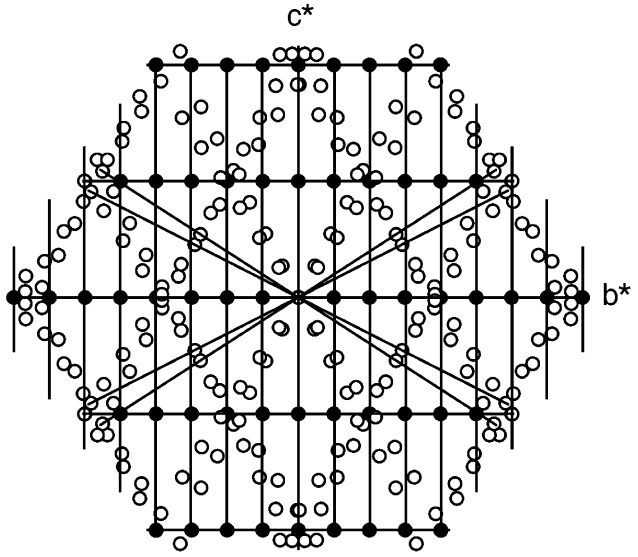

Fig. 12. [100]* view of the reciprocal lattices of γ-MnO_2 with $b/(2c) = 1.635$ (filled circles) and its orientation variants (open circles), each variant resulting from ideal twinning; The [001]* directions in the variants are drawn, at ca. 60/120° from c^*.

rich'' PXRD patterns, for instance, the EMDs obtained using a moderate or small DCD, and most of the CMD's. Here, the main factors to be considered, because of their relationship with the diffraction patterns, are:

- the size of the perfect, ordered domains (still ignoring Pr);
- the features of the twin boundaries (are they well-defined? are they the twin planes? parallel?, etc.).

4.3.1. *Increase of the order from SRO*

This possibility leads to a structural image of SRO probabilities extended to third, fourth, fifth, etc. neighboring Mn rows, thus giving microdomains without well-defined boundaries. The local symmetry then becomes orthorhombic within a microdomain.

In reciprocal space, the symmetry should remain hexagonal, and we expect that the diffuse intensity increases in the regions near the points, which will become reciprocal lattice points at the limit of macrotwinning. As a possible supporting observation, we point out that in the PXRD pattern of an EMD, the intensity near ca. 22° regularly varies when the DCD varies, from a small bump (at the highest DCD) to a strong line, whose the width is explained simply by the presence of De Wolff defects together with a size effect (at the smallest DCD).

However, more complicated situations could exist, for instance with imperfect hexagonal symmetry, as crystals of EMD grow in an anisotropic medium.

4.3.2. *Occurrence of numerous, parallel (021) or (061) twin planes in the structure*

A microtwinning due to parallel (021) twin planes (or as well (061) planes, which give similar effects [3] in PXRD) is a rather attractive model if the direction of growth $\boldsymbol{\Gamma}$ of the ''crystals'' is [021]* (or [061]* for (061) twin planes) during the electrochemical deposition.

Studies of texture and structural anisotropy were performed by XRD for EMDs [13,14,16]. Considering Figs. 11–13 in Ref. [16], the direction of growth $\boldsymbol{\Gamma}$ of most EMDs seems to be of the type $[110]^*_H$, i.e., a type of direction which should correspond in twinned R to both [061]* and [001]* types of direction. Note that $\boldsymbol{\Gamma}$ is thus not along a [021]* type of direction, in contrast with a previous hypothesis [2]. The conclusion of the XRD study of De Wolff [14] is consistent with the present interpretation, as it states that the a_H-axis of the hexagonal ε-MnO_2 is along $\boldsymbol{\Gamma}$ (note it is however difficult to accept all the conclusions in Ref. [14], as they imply both a hexagonal symmetry and an a_H-axis which is not fully equivalent to b_H). In contrast, other authors did not detect, by XRD, any preferred orientation in a bulk production EMD [13]. If the conclusion of De Wolff is retained (axis a_H is along $\boldsymbol{\Gamma}$), the c-axis of corresponding R is either along $\boldsymbol{\Gamma}$, or at ca. 60° from $\boldsymbol{\Gamma}$.

Whatever the preferred orientation, the twinning models considered are those for which PXRD and SAED patterns have been calculated, thus leading to classifications of the γ-MnO_2s [2,3,5]. Fig. 13 shows consequences of the twinning in reciprocal space; it holds for any value of h. The broken lines indicate the locations of the resulting streaks and calculations of the intensity were performed along all these lines. All the nodes on these lines undergo broadening and are shifted along the streak. Arrow A in Fig. 13(a) indicates particular cases, in which couples of close lattice points appear. Such a couple corresponds to intense reflections from two equivalent orientation variants, for instance $h21$–$h40'$ or $h61$–$h02'$, as already described [2]. Figs. 14–16 show examples of the intensity calculated along the streaks, which are marked by broken lines in Fig. 13. As illustrated by Fig. 17, similar results are found for r, and therefore for the intergrowths of R and r. For twinning (061), similar streaks, broadening and shifts are observed along the broken lines of Fig. 13(b). Note that the variations of the intensities at increasing α do not depend on the value of the index h, and that the shifts observed do not result from a variation of the unit-cell parameters.

Fig. 14 shows that the shift of intensity is rapid for a couple of close nodes in Fig. 13, while Fig. 16 shows that for other cases the prevailing evolution upon twinning is the broadening rather than the shift.

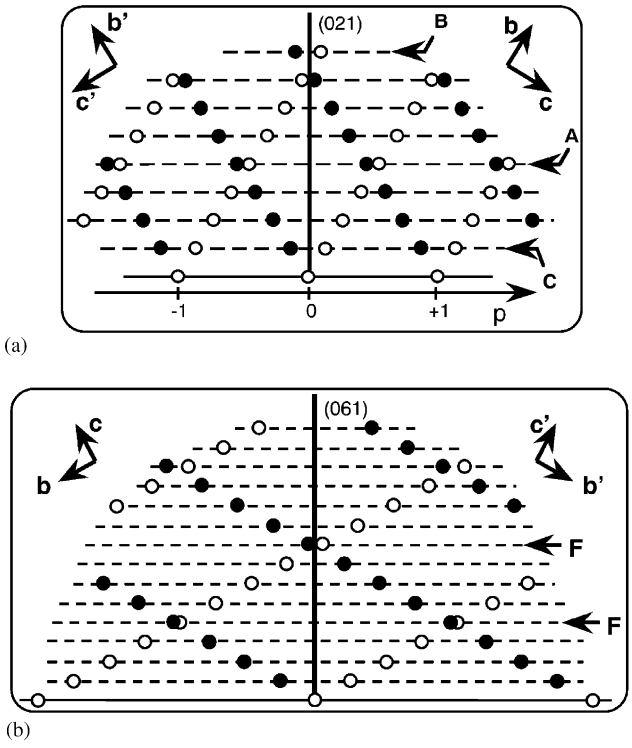

Fig. 13. [100]* views of the reciprocal lattices in the case of (a) (021) or (b) (061) twinning in R. Arrows A and F show particular couples of close lattice points, see text.

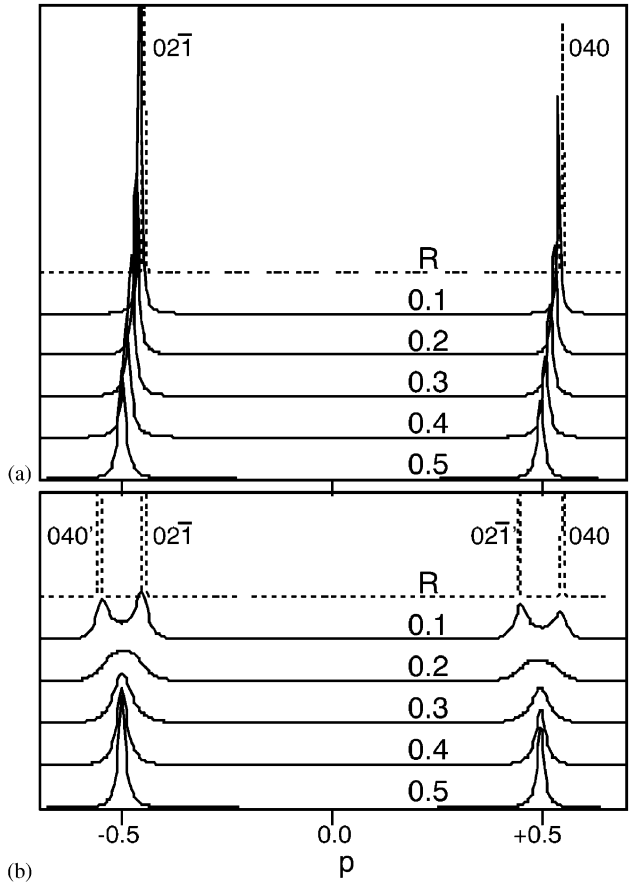

Fig. 14. Intensity in reciprocal space, at $h = 0$, along the streak indicated by arrow A in Fig. 13, for (021) twinning in R, with (a) Tw model, (b) Mt model. The probability α is indicated. Coordinate p is defined in Fig. 13. The shape of the curves does not depend on h.

The two previous models associated with Tw [2] or Mt [3] lead to rather similar consequences of the twin planes considered here in the calculated PXRD patterns. In reciprocal space, however, the situation is theoretically quite different, as illustrated by Figs. 14–17. With the Tw model, a single reciprocal lattice is progressively modified when the twin probability α increases, while with the Mt model two reciprocal lattices of two equivalent twin domains progressively coalesce. The result is the same for $\alpha = \frac{1}{2}$.

An important point to be underlined is that, for both the models (with Tw or Mt), significant spot broadening and shifts, and probably streaking, could be observed even when $h = 0$, i.e., in the (b^*, c^*) plane which is a reciprocal plane rather easy to find and recognize in a SAED study. Fig. 15 shows a case for which a significant broadening is expected with both models. Considering Figs. 14–17, it is difficult to predict whether the streaks would be observable in a SAED pattern. At least the broadening, however, should be observable.

Fig. 18 tries to summarize what may be detected during a SAED study by giving schematic representations of the streaks, broadenings and shifts which should then appear in the pattern for a [100] zone, when all the twinnings are present. Only the reflections of significant intensity are represented on the figure, which try to take into account, in the results, the common features of Figs. 14–17.

4.3.3. Simultaneous occurrence of numerous, parallel (021), (20$\bar{1}$), (061) and (06$\bar{1}$) twin planes in a "crystal"

The hypothetical situation here implies "perfect" domains (the De Wolff defects are still ignored) which are necessarily small, so that the obtained image of small domains with various boundaries is not far from the image of the SRO microdomains already considered. The hexagonal or orthorhombic character of the structure could be difficult to distinguish. It seems to be the case for a CMD in Ref. [15], in which the SAED pattern in Fig. 6a exhibits hexagonal symmetry, whereas that of Fig. 6c, from the same crystal, after rotation about $[100]^*_H$, looks to be a [101] zone of an orthorhombic γ-MnO_2.

We expect that the size of the domains and the features of the twin boundaries are crucial, as at a nanometer scale most of the Mn atoms are close to a

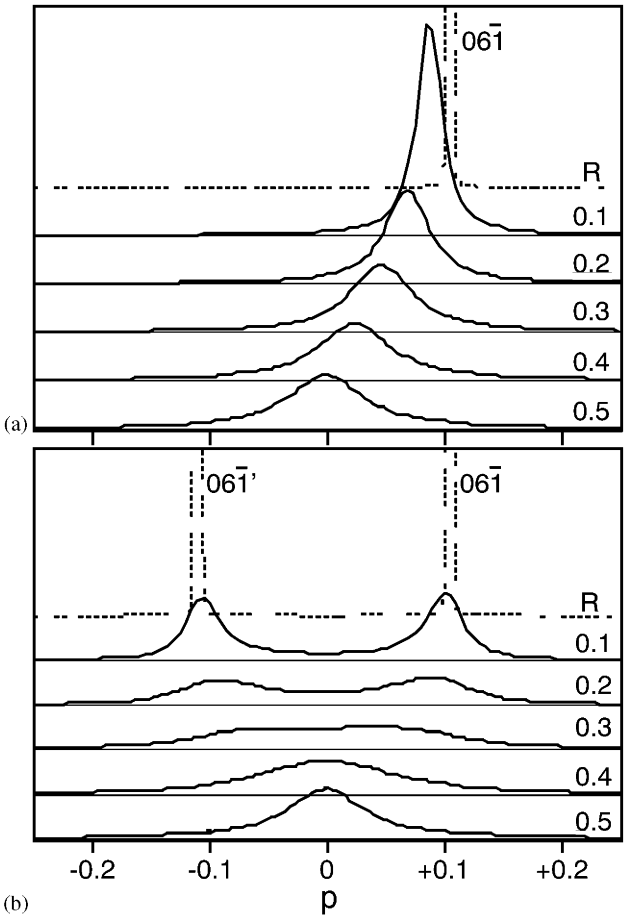

Fig. 15. Same as Fig. 14, for arrow B in Fig. 13.

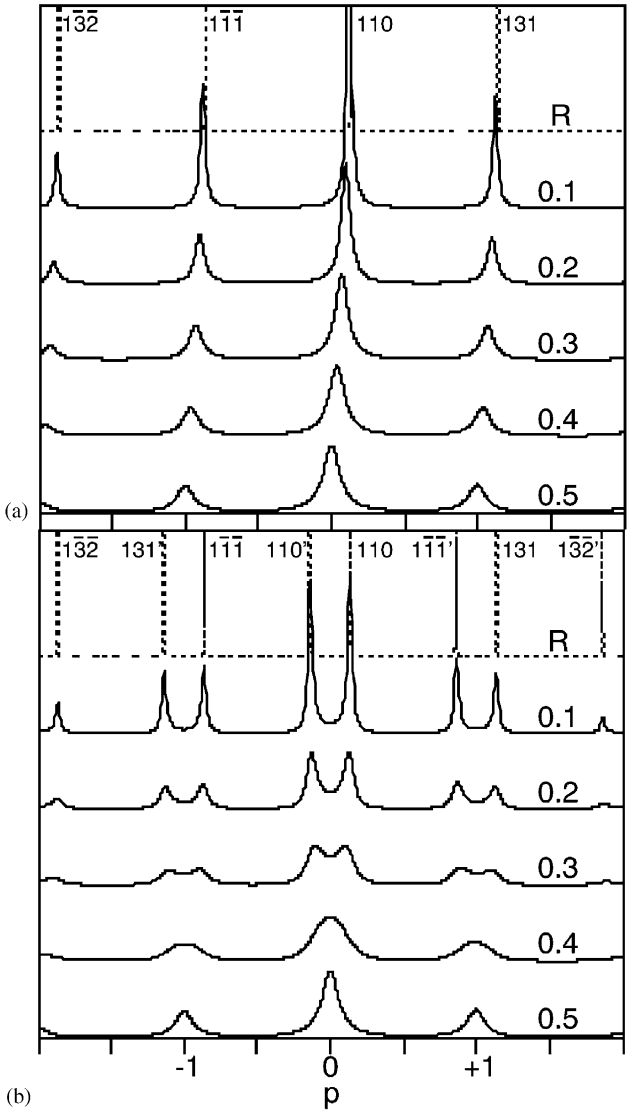

Fig. 16. Same as Fig. 14, for arrow C in Fig. 13 and for $h = 1$.

boundary, thus having an environment somewhat influenced by the microtwinning. As a consequence, the smaller the size of the domains, the greater the probable modification of the periodicity parameters due to twinning, in particular the $b/(2c)$ ratio. It was remarked in Ref. [2] that most of the CMD's correspond to $b/(2c) \approx 1.66$, and we often obtained a value close to 1.66 during our SAED study of γ-MnO_2s. As already pointed out, 1.66 is greater than the value for R (1.617) and for r (1.531).

Not only may the periodicity be modified by the microtwinning, when the boundaries between the orientation variants coincide with the twin planes. The relative orientation of neighboring domains is expected to slightly change, with respect to the case of macrotwinning, to make possible the simultaneous optimization of the structure of all the boundaries and all the twin-related domains. This small change must exist in the case of non-hexagonal symmetry, as two neighboring twin domains do have slightly different orientations when they are related to a third one by perfect, ideal (021)/(061) twinning, as illustrated by Figs. 12 and 19. Fig. 12 shows that the difference between close ideal orientations is small (a few degrees), and arrows A in Fig. 19 show an example of regions where some relaxation (involving both orientation and periodicity) is necessary to ensure an acceptable structural continuity. Since the small differences in orientation above depend on the value of $b/(2c)$, a relationship exists between the microtwinning discussed here and both the periodicities and the relative orientations of the various twin domains. In reciprocal space, the relaxations correspond to reciprocal lattices, which become as close as possible to each other for all the domains. Figs. 20(a)–(d) represent, in reciprocal space, the intensity expected in the planes $h = 0$ or $h = 1$, without relaxation (see Figs. 20(a), (b) arbitrarily drawn for $b/(2c) = 1.635$), or with relaxation (see Figs. 20(c),

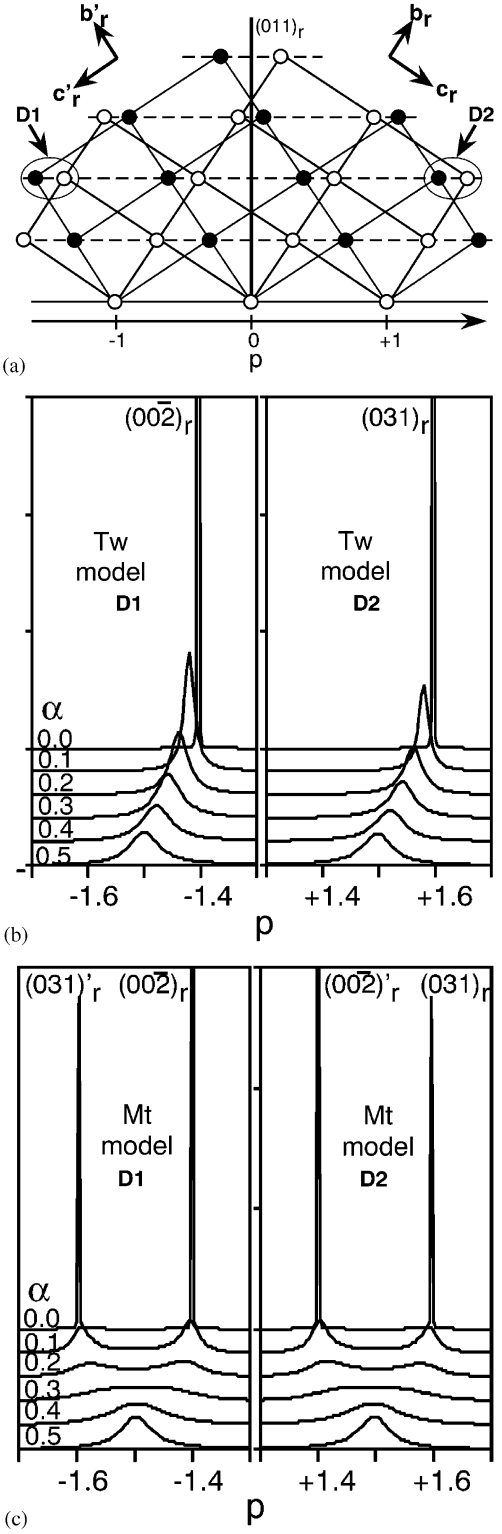

Fig. 17. Homologues of Figs. 13(a) and 14 for r instead of R. Note the analogies. The major consequences of twinning in R concern r and γ-MnO_2 also.

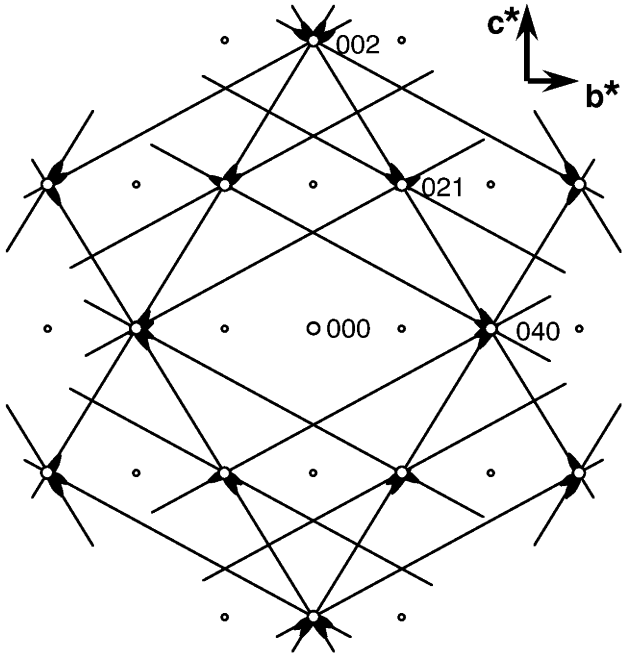

Fig. 18. Schematic representation of the SAED pattern of zone [100] expected in the case of "parallel twinning" (see the text). The lines indicate possible streaks. The dark elongated marks try to represent all the possible directions of broadening and shifts.

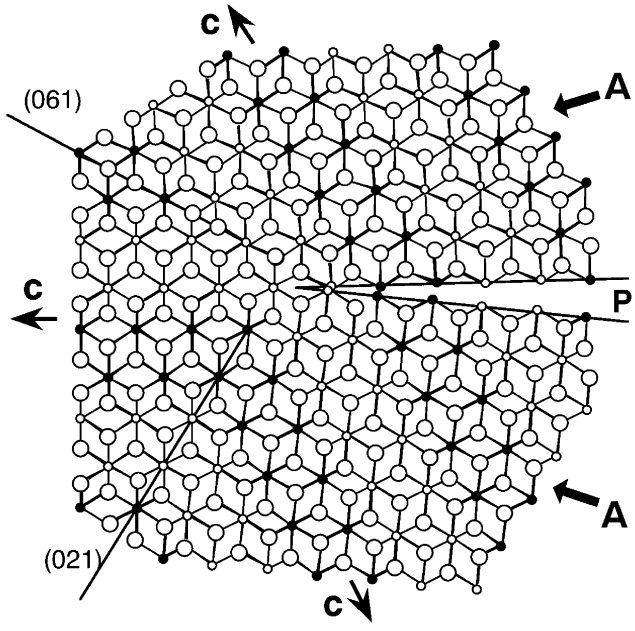

Fig. 19. Schematic [100] view of two hypothetical, ideal, adjacent orientation variants (arrows A) resulting from (021) and (061) twinning. A relaxation is necessary to ensure a structural continuity in region P. Axes *c* indicate the directions of the chains of octahedra.

(d) drawn for $b/(2c) = 1.66$). In Fig. 20, the weakest reflections are omitted for clarity. Without supporting calculations, we cannot state whether significant streaking should be added or not in Fig. 20 (the possible streaks would be those shown in Fig. 18).

Figs. 20(a), (c) show the splitting of spots, which may be directly observed in a [100] zone by SAED. At $h = 1$,

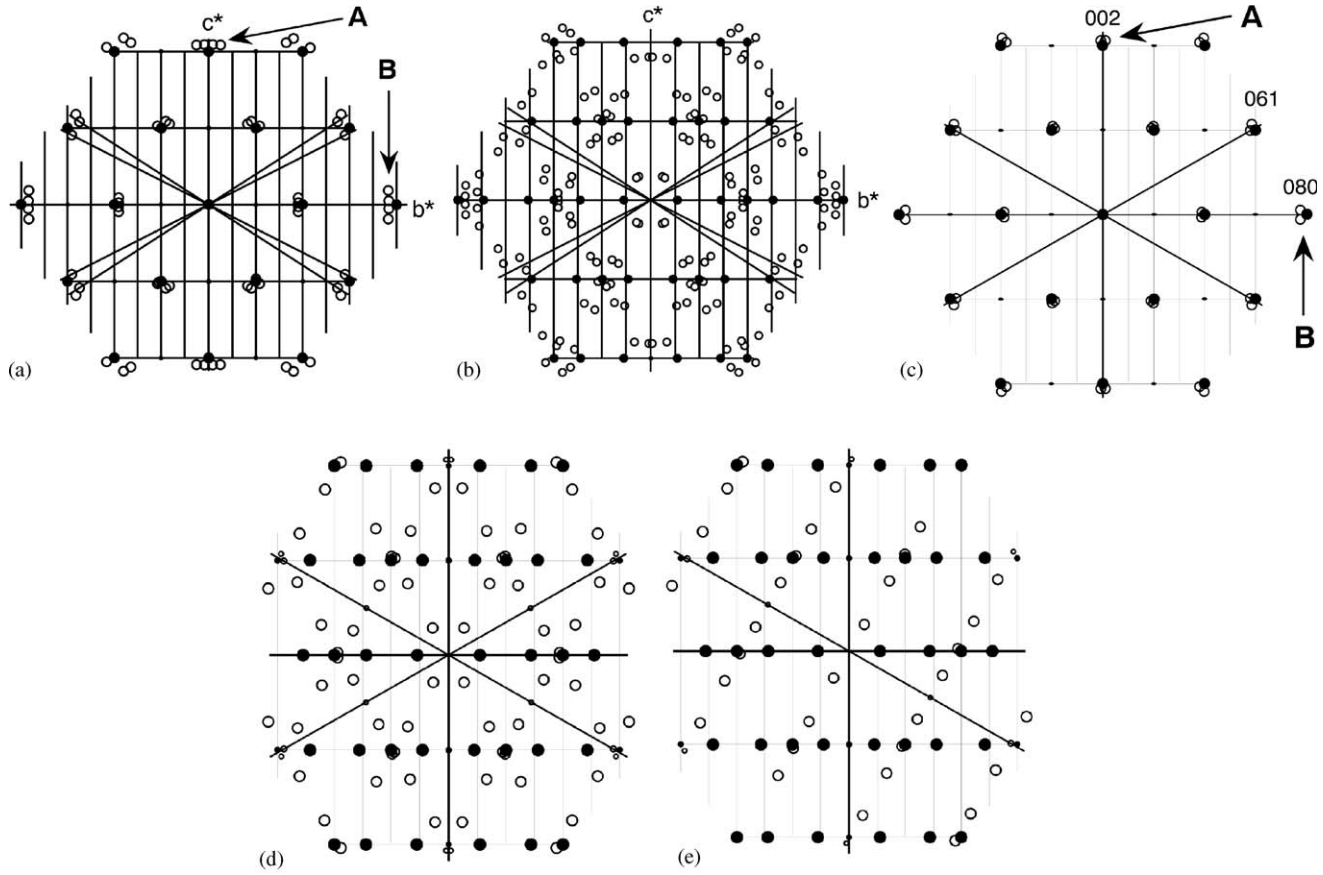

Fig. 20. (a) and (b) schematic drawing of the expected reciprocal planes inferred from Fig. 12, at $h = 0$ (a) and $h = 1$ (b), removing the weak reflections, with $b/(2c) = 1.635$; (c) and (d) are drawn for $b/(2c) = 1.66$, adding a relaxation by rotation (see the text), for $h = 0$ and $h = 1$, respectively; (e) is the same as (d) with one of the orientation variants removed. In (b), (d) and (e), the relevant circles are slightly shifted to take into account the presence of De Wolff defects.

the features shown by Figs. 20(b), (d) cannot be revealed by just a single electron diffraction pattern.

5. SAED study—results and discussion

5.1. Remarks on the samples and on the crystals

The samples selected for the SAED study are EMDs giving PXRD patterns similar to those in Fig. 3, i.e., they are of relatively good crystallinity, with $Pr \approx 0.4$. The two lines 221 and 240 in the 2θ range 56–60° are well resolved into two peaks, thus revealing a low microtwinning rate ($Tw \approx 25$, $Mt \approx 20$). The SEM images of the surface show that the electrochemical deposits clearly consist of needle-like or rod-like fibers, or of bundles made of small fibers [4].

However, after the grinding required to prepare the grid for the TEM study, the morphology is generally strongly modified, as illustrated by Fig. 21. In one case (sample A in Fig. 3), the needle-shaped aspect of the crystals was more pronounced in the TEM images than in Fig. 21.

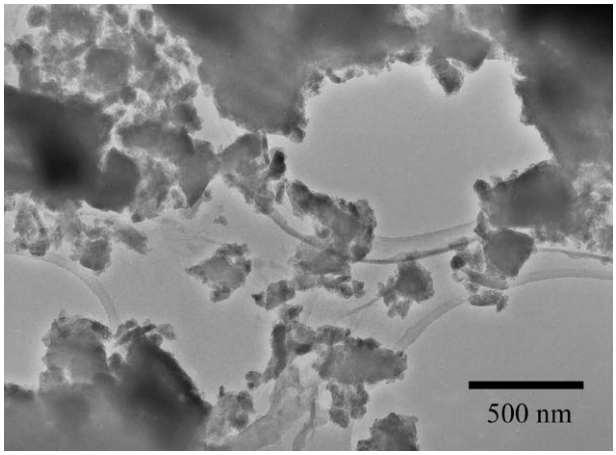

Fig. 21. Bright field TEM image of sample B (see Fig. 3).

Let us refer to a "fragment" as a crystal, a grain, or a region of them selected for a SAED study. Many fragments were considered, in several samples, and most of them are polycrystals difficult to thoroughly study. To obtain reliable results, most of the fragments selected

had the appearance of single crystals, preferably with a simple shape and with a clear direction of elongation. When it was identified, this direction was always that of [001].

5.2. Features due to the De Wolff defects

A few SAED patterns were taken, starting from the [100] zone, after rotation about [010]*, to verify the shifts expected [2,6,7]. The shifts are qualitatively described in Fig. 22. The experimental shifts directly observed by SAED are illustrated by Fig. 23. They agree with the previous results (see for instance Fig. 2b in Ref. [7]) and with the practical effects already shown by Figs. 3, 5 and 6. The shifts have been qualitatively taken into account in drawing Figs. 20(b), (d), (e), i.e., for $h = 1$ and not for $h = 0$ for the following reasons:

(i) as we discussed earlier, a weak effect should occur at h even;
(ii) Fig. 6 clearly shows strong effects for $h = 1$;
(iii) all our reliable SAED results show shifts, which concern h odd only.

As shown by Figs. 6 and 23(a), (b), the De Wolff defects, which are planar defects, provoke shifts, broadening, and streaks parallel to [010]*.

5.3. Evidence for twinning from the [100] zone

For each fragment considered, the [100] zone was systematically searched with the aim of detecting the splitting of spots such as in Figs. 20(a), (c). A pattern was generally taken with the condenser lens strongly defocused, during a study of the corresponding reciprocal lattice. Various situations were then observed, revealing a lack of homogeneity at a microscopic scale. The values of the ratio $b/(2c)$ directly inferred from orthorhombic [100] zones were found to be in the range 1.62–1.70, i.e., a range which implies a large range of twinning rates. Fig. 24, for instance, reveals very different fragments, since that of Fig. 24(a) is a

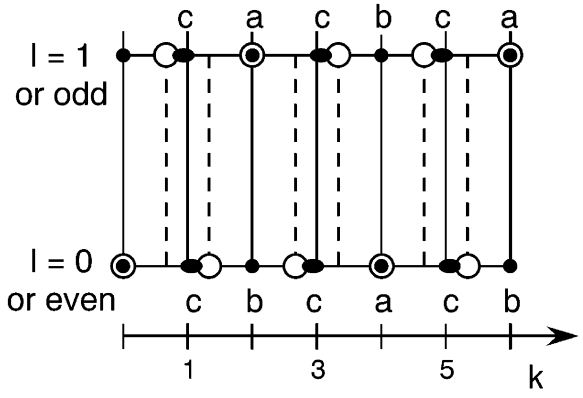

Fig. 22. Effects of the De Wolff defects in R: when Pr increases, a reciprocal lattice point of R(filled circle or ellipse) (a) is not perturbed; (b) progressively disappears; (c) is shifted toward the close lattice point of the HOMD (open circle).

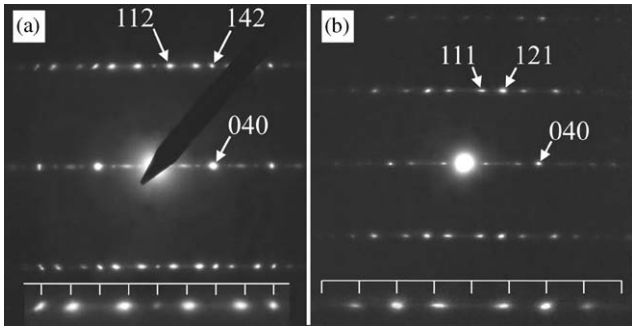

Fig. 23. SAED patterns showing the shifts of intensity due to the De Wolff defects for: (a) $l = 2$, in a [20−1] zone; (b) $l = 1$, in a [10−1] zone. The insets show enlarged details and periodic ticks for comparison (see also Figs. 6 and 22).

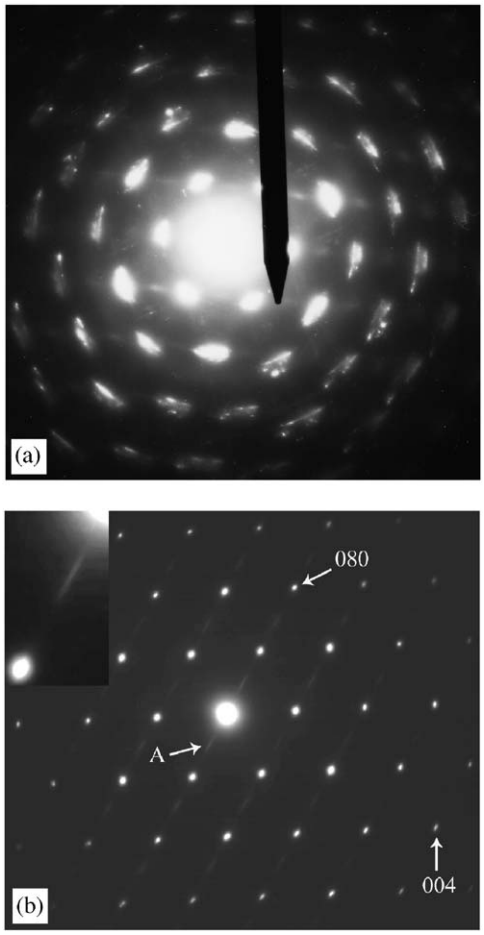

Fig. 24. SAED patterns of: (a) a polycrystal with a fibrous texture; (b) a [100] zone with fine spots and streaks. The inset shows region A enlarged. $b/(2c) = 1.657$.

polycrystal exhibiting a fibrous texture with at least [100] as a common axis of preferred orientation, while Fig. 24(b) reveals fine spots without any splitting, which disappear rapidly upon rotation of the crystal. In Fig. 24(b), the inset is region A, enlarged to show that in zone [100] the reflections with $k/2+l$ odd appear as weak spots elongated parallel to [010]*. For other fragments, the latter spots are often less intense and less elongated. In all cases, they unambiguously indicate which are the [010]* and [001]* directions. Patterns such as that of Fig. 24(b) were often observed in the case of an acicular fragment.

In Fig. 25, the geometrical symmetry of the [100] zone is close to hexagonal ($b/(2c) = 1.70$) and, apart from a very weak splitting of several spots revealing a small rotation about the zone axis, there is no real evidence for any other splitting of spots. The value 1.70 being close to $\sqrt{3}$, the microtwinning rate is likely high, which is in fair agreement with the TEM image of the corresponding fragment (Fig. 26). When the value $b/(2c)$ is close to $\sqrt{3}$, the splitting is of course less than in Figs. 20(a), (c), and it is likely not detected.

The whole set of features of Fig. 20(a) or (b) has not been unambiguously observed in a single pattern. Splitting, however, clearly appears on many patterns, as illustrated by Figs. 27–29. Qualitatively, the splitting observed corresponds well to those of Figs. 20(a), (c); in particular, regions of spots 040 (Fig. 28) and 002 (Fig. 29) are similar to regions B and A in Figs. 20(a), (c). Note that the broadening in Fig. 18 has never been observed, so that a significant "parallel" microtwinning is unlikely.

In Fig. 30, the symmetry is hexagonal near the center of the [100] zone, and splitting appears near the

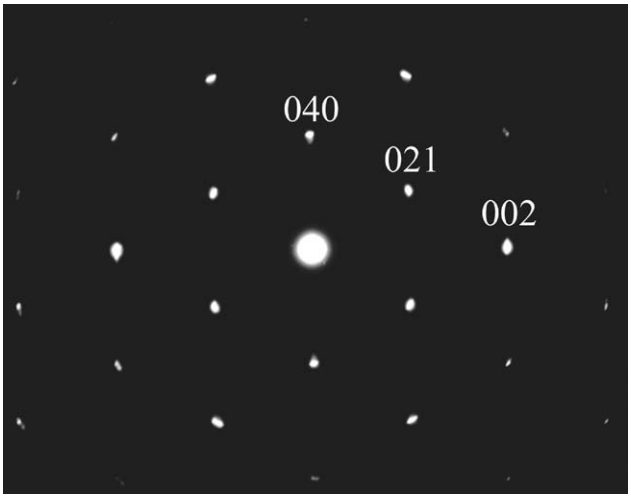

Fig. 25. SAED pattern: [100] zone of the fragment in Fig. 26. The symmetry is close to hexagonal ($b/(2c) = 1.70$).

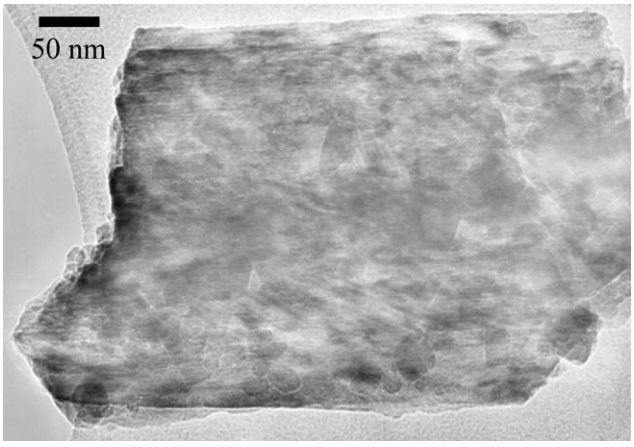

Fig. 26. Low-resolution bright field image of a fragment slightly elongated along [001]. Note the many, irregular domains.

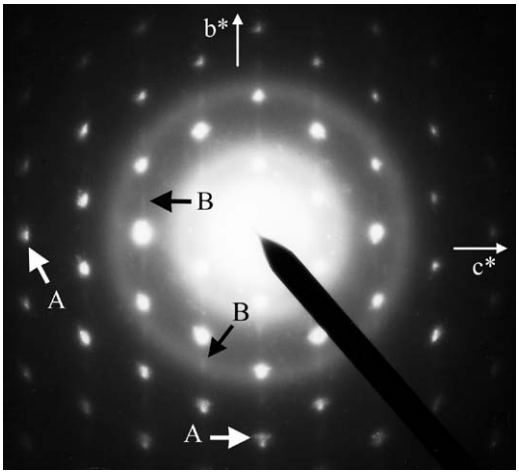

Fig. 27. SAED pattern: [100] zone similar to a hexagonal $[001]_H$ zone. The streaks (see, for example, arrows B) indicate the direction [010]*. Arrows A show split spots.

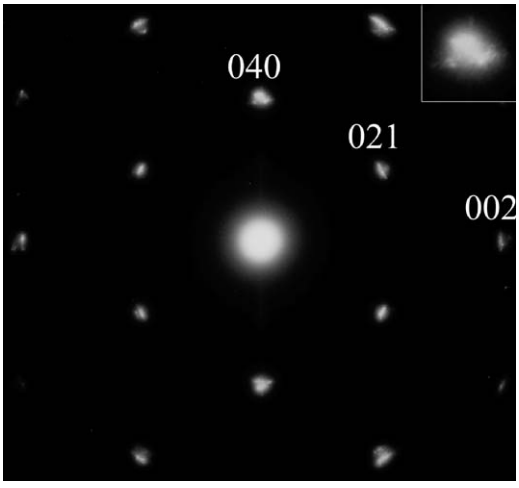

Fig. 28. SAED pattern: [100] zone with $b/(2c) = 1.62$ for the set of intense spots. Close, weaker spots also appear and, as an example, the inset shows the detail of the split spot 0 4 0.

periphery. Since the streaks indicate the directions of R–r intergrowth, the real, local symmetry is orthorhombic and the nearly hexagonal symmetry comes from the twinning. The splitting of spots, however, does not obey the hexagonal symmetry, nor any symmetry. Therefore the splitting and the images of the fragment (Fig. 31) have not been truly understood probably due to small fluctuations of the orientation within each orientation variant.

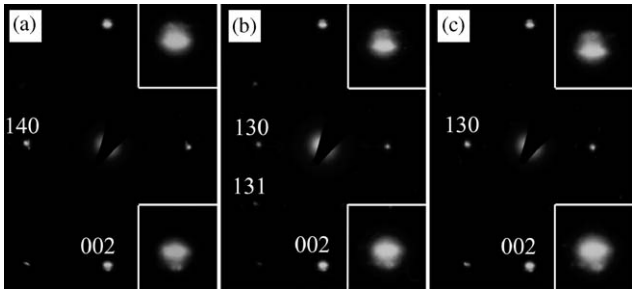

Fig. 29. SAED patterns showing the splitting of spots 0 0 1 during a rotation about [001]*. The insets show these spots enlarged.

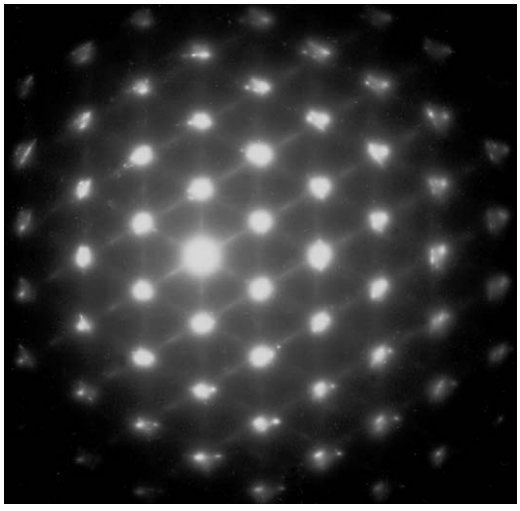

Fig. 30. Evidence for the existence of three equivalent orientation variants, each with an orthorhombic symmetry, in the fragment, while the symmetry of the central part of the pattern is hexagonal. The streaks reveal three directions for the De Wolff defects.

5.4. Evidence for diffuse intensity due to microtwinning

In addition to the streaking, broadening and shifts parallel to [010]*, associated with the De Wolff defects, the SAED studies reveal diffuse intensity in reciprocal planes parallel to the [100] zone. As illustrated by Fig. 32, the diffuse intensity is negligible at h even and significant at h odd, the maximum being for $h = 1$. A diffuse plane at $l_H = 1$ was already mentioned [15] for a hexagonal ε-MnO_2. During the present exploration of the reciprocal space by rotation about [001]*, the diffuse plane $h = 1$ was revealed by streaks parallel to [001]*, intersecting $1kl$ reflections in the SAED patterns. Fig. 33 shows examples. The (numerous) weak spots result from the intersections of the streaks parallel to [010]* with the Ewald's sphere (see also Fig. 34).

Fig. 35 shows that the diffuse plane can be inferred from the intersections of the patterns (arrow A) with the plane $h = 1$ (arrow B). The intersections (broken lines, arrow C) are the successive streaks. Figs. 35–37 show such a set of streaks and schematic representations of the planes. Fig. 37 summarizes the results for several fragments, indicating by circles or ellipses all the regions where reinforced intensity was observed in the plane $h = 1$. Note that these regions are not located with precision and the diffuse intensity becomes weak or negligible when $k > 4$.

The aspect of the additional intensity at $h = 1$ depends on the fragment considered, as illustrated by Figs. 38 and 39. In Fig. 38(a), arrow B shows a slightly elongated spot, while A indicates intensity forming a streak. In contrast, in Fig. 38(b), the intensity is not very different at A and B. In Fig. 39, the aspect is still different and the shape of the fine spots at B are nearly those expected in the case of macrotwinning.

In Fig. 33, the intensities at D and E are different. This lack of symmetry has been observed on most of the streaks (see also Fig. 36). Note also that the distance

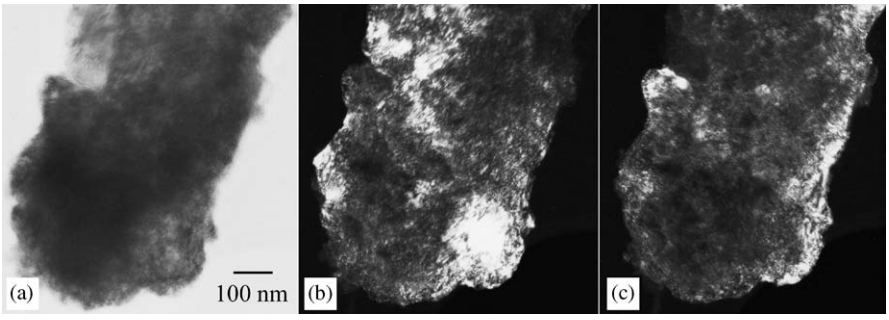

Fig. 31. Low-resolution images of the fragment corresponding to Fig. 30: (a) bright field image; (b) and (c) dark field images using spots $1\,0\,0_H$ and $0\,1\,0_H$, respectively.

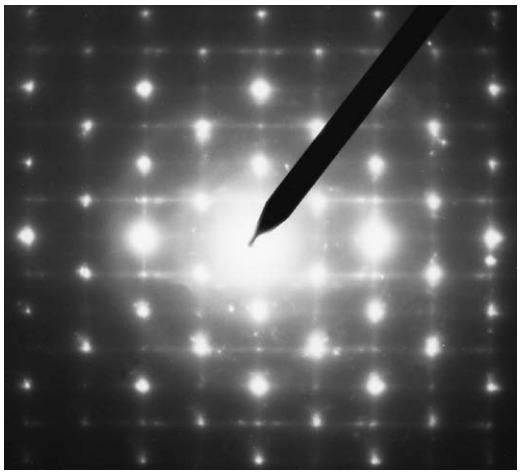

Fig. 32. SAED pattern taken with a long-time exposure, after rotation of ca. 4° about [001]* starting from the [010] zone. The intense, horizontal streaks are parallel to [001]* and correspond to h odd.

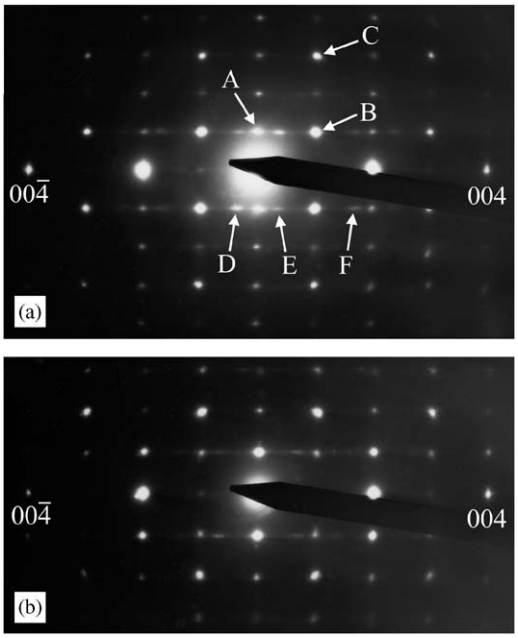

Fig. 33. Additional streaks and diffuse intensity in SAED patterns; (a) and (b) correspond to orientations c and e of Fig. 34, respectively. A: diffuse intensity due to De Wolff defects; B and C: reflections 111 (shift taken into account) and 321; D, E and F: additional intensity on a streak.

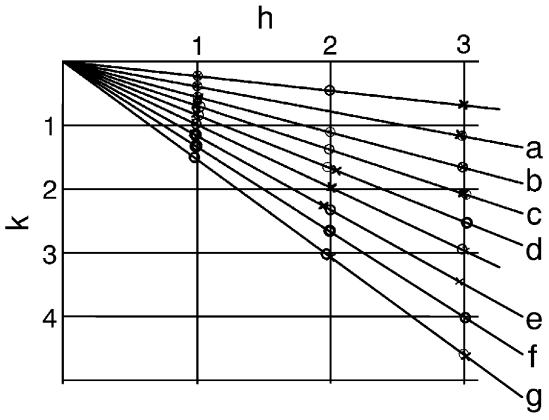

Fig. 34. Examples of patterns taken during a SAED study with rotation about [001]*. The marks represent observed intersections with the streaks which are parallel to [010]*.

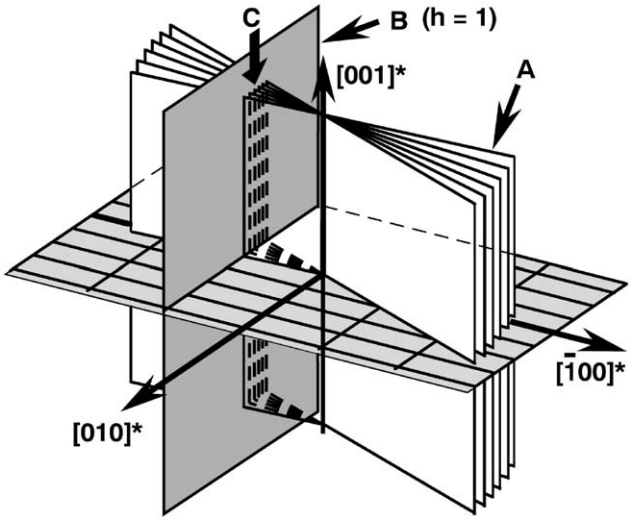

Fig. 35. Each pattern (arrow A) intersects the diffuse intensity plane (arrow B) along a streak (arrow C).

from D to F is slightly greater than $2c*$; this feature has been remarked on several patterns and Fig. 38(b) shows a clear example. In agreement with the latter observation, a comparison of Figs. 20(b) or (d) and 37 shows that the additional intensity is located near (or at) reciprocal lattice points expected in the case of twinning. In fact, due to the frequent lack of symmetry mentioned above, the intensity observed generally corresponds to a figure intermediate between Figs. 20(d) and (e), with of course diffuse intensity instead of fine spots. The broadening, streaking and shifts expected in the case of "parallel" microtwinning were not detected.

The present results give evidence for twinning and microtwinning revealed by particular additional intensity in reciprocal space. This intensity varies from rather sharp spots, which is interpreted as coming from extended orientation variants, to diffuse intensity, which likely comes from a number of nanometric twin domains. Of course, the size, number and proportions of the different types of domain determine the extension, magnitude and symmetry of the diffuse intensity.

As the strongest SAED intensity corresponds to a single reciprocal lattice, in which supplementary (weaker), diffuse intensity exists, we propose a structure with twin domains embedded in a "normal" structure (with De Wolff defects). As the diffuse intensity itself is part of

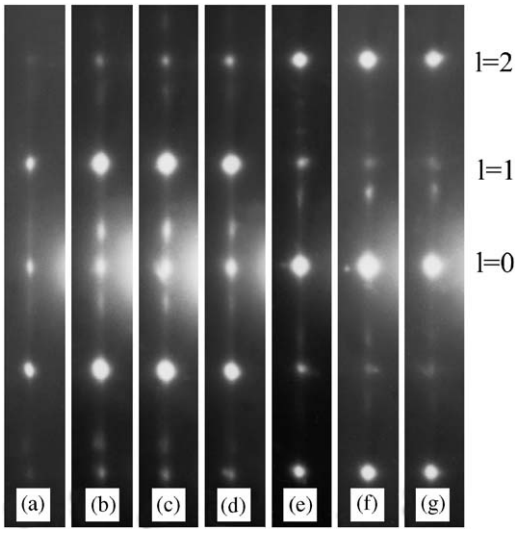

Fig. 36. Intensity on the set of streaks at $h = 1$ on patterns a–g (see Fig. 34 and arrows C in Figs. 35 and 37).

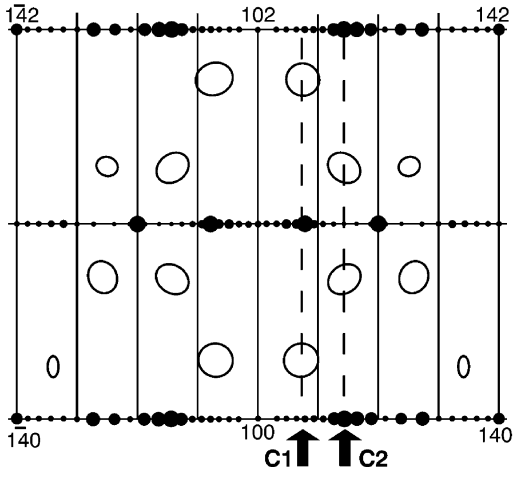

Fig. 37. Schematic representation of the intensity in a part of the reciprocal plane $h = 1$. The whole plane contains diffuse intensity. Circles and ellipses mark the regions of reinforced intensity observed. Arrows C1 and C2 correspond to patterns a–d and e–g, respectively, in Figs. 34 and 36. The dark disks correspond to "normal" intensity with shifts and streaking due to De Wolff defects.

a diffuse plane, and as the streaks in Fig. 18 have not been detected, we suppose that the boundaries of these domains are not always the twin planes. They are likely boundaries containing various types of other defects, which produce the diffuse intensity plane at $h = 1$.

6. Concluding remarks

Precise and reliable SAED studies were performed for rather well crystallized γ-MnO_2 samples. When it was unambiguously determined, the axis of elongation of the crystals was along [001].

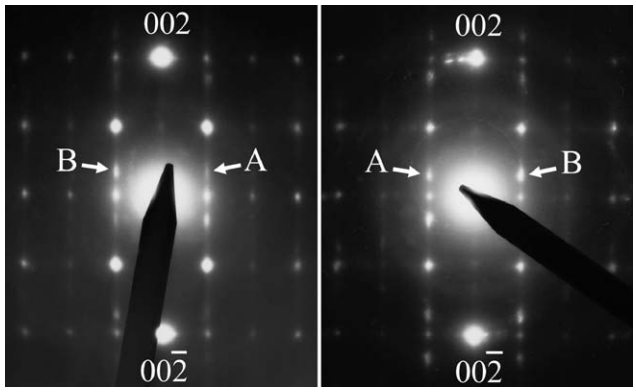

Fig. 38. SAED patterns, from two different fragments, the orientation of which is nearly that of pattern b in Fig. 34. The intensity is less, and more diffuse, at A as compared to B.

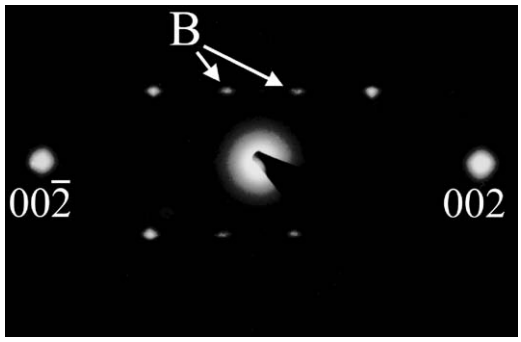

Fig. 39. For an orientation close to that involved in Fig. 38, the additional intensity (arrows B) is not diffuse in this pattern.

For the microtwinning, the previous calculations assumed a "parallel" microtwinning, i.e., parallel twin planes and twin boundaries in these planes. Although the previous classifications by the parameters (Pr, Tw) or (Pr, Mt) still remain quite useful, the SAED results do not confirm the model of "parallel" microtwinning and they lead to the proposition of the existence of twin domains, likely with complicated contours. At low twinning rate, the domains appear to be included in the "normal" structure (the r–R intergrowth). The increase of the twinning rate would be an increase of the number of domains (possibly with a decrease of the domain size) and thus a progressive, continuous trend to SRO for Mn, the extreme limit being the "true" ε-MnO_2.

As the microtwinning must modify the mean periodicity of the structure, the ratio $b/(2c)$ remains an attractive parameter for the estimation of the real twinning rate. However, as the "parallel" microtwinning model is not confirmed, its effects are questionable; they are taken into account in the previous classifications and they should be reconsidered. The next step should be a

HRTEM study showing the domains and the features of their boundaries. [100] is probably the best direction of observation for this study. Then, further work should be a modification of the previous methods allowing both the classification in the whole γ-MnO_2 family and good agreement with the real structures.

References

[1] D.G. Malpas, F.L. Tye, Handbook of Manganese Dioxides Battery Grade, In: D. Glover, B. Schumm Jr., A. Kosawa (Eds.), IBA Inc & JEC Press Inc., Brunswick, 1989 (Chapter V).

[2] Y. Chabre, J. Pannetier, Prog. Solid State Chem. 23 (1995) 1–130.

[3] S. Sarciaux, Ph. D. thesis, University of Nantes, Nantes, France, 1998.

[4] L.I. Hill, A. Verbaere, D. Guyomard, J. Power Sources 119–121 (2003) 226–231.

[5] L.I. Hill, A. Verbaere, D. Guyomard, J. Electrochem. Soc. 150 (2003) D135–D148.

[6] P.M. De Wolff, Acta Crystallogr. 12 (1959) 341.

[7] J.-C. Charenton, P. Strobel, J. Solid State Chem. 77 (1988) 33–39.

[8] S. Turner, P.R. Busek, Nature 304 (1983) 142.

[9] L.I. Hill, A. Verbaere, D. Guyomard, J. New Mater. Electrochem. Systems 5 (2002) 129–133.

[10] W. Kraus, G. Nolze, Federal Institute for Materials Research and Testing, Berlin, Germany, 1999.

[11] M.M. Treacy, J.M. Newsam, M.W. Deam, Proc. R. Soc. London A 433 (1991) 499.

[12] A.M. Byström, Acta Chem. Scand. 3 (1949) 163.

[13] A.H. Heuer, A.Q. He, P.J. Hughes, F.H. Feddrix, ITE Letters on Batteries, New Technol. Med. 1 (2000) 926–930.

[14] P.M. De Wolff, J.W. Visser, R. Giovanoli, R. Brütsch, Chimia 32 (1978) 257–259.

[15] P. Strobel, J.-C. Joubert, M.-J. Rodriguez, J. Mater. Sci. 21 (1986) 583–590.

[16] E. Preisler, J. Appl. Electrochem. 6 (1976) 301–310.